Journal of Alloys and Compounds 918 (2022) 165606

Contents lists available at ScienceDirect

Journal of Alloys and Compounds

journal homepage: www.elsevier.com/locate/jalcom

Research Article

Evolution of lamellar architecture and microstructure during redox cycling of Fe-Co and Fe-Cu foams

Samuel M. Pennell*,[1], Jacob B. Mack[1], David C. Dunand

Department of Materials Science & Engineering, Northwestern University, 2220 Campus Drive, Evanston, IL 60208, USA

ARTICLE INFO

Article history:
Received 6 April 2022
Received in revised form 18 May 2022
Accepted 24 May 2022
Available online 26 May 2022

Keywords:
Energy storage materials
Metals and alloys
Sintering
X-ray diffraction
Oxide materials

ABSTRACT

The effects of alloying Fe with 25 at% Co or 30 at% Cu are studied in freeze-cast lamellar foams subjected to redox cycling under H_2- and H_2O-rich atmospheres at 800 ºC, relevant to metal-air batteries. In unalloyed Fe foams, redox cycling causes irreversible Kirkendall porosity growth within lamellae, leading to fracture and buckling in the lamellar architecture which in turn leads to foam densification after a few cycles. By contrast, Fe-25Co lamellae develop, upon oxidation, a pure Co core and a Fe_3O_4 shell which decreases buckling and Kirkendall pore growth, thus slowing sintering and densification of the lamellar foams. After Fe_3O_4 reduction, the Fe-rich shells and Co-rich cores of the lamellae re-homogenize by diffusion to the original single-phase Fe-25Co alloy, achieving a reversible microstructure upon a full redox cycle. After 10 cycles, average channel porosity (between lamellae) undergoes only a small decrease (from 62 % to 46 %), with minimal Kirkendall pore coarsening in the lamellae, consistent with strong sintering resistance in the Fe-25Co foams. The Fe-30Cu foams also display lamellae with Cu core and a Fe_3O_4 shell structure after oxidation, since Cu, like Co, does not oxidize under steam. However, the lack of solubility of Cu in Fe prevents re-homogenization after Fe_3O_4 reduction, so the resulting Cu-core / Fe-shell lamellae undergo severe sintering and densification upon subsequent redox cycling, with channel porosity reducing from 61 % to 9 % after just 5 cycles. For both systems, *operando* x-ray diffraction during redox cycling reveals that Cu, unlike Co, doubles the Fe oxidation rate, as compared to pure Fe foams.

1. Introduction

Metal-air battery systems are promising candidates for large-scale, inexpensive energy storage since the use of a gaseous species - such as ambient air or steam - as the reaction mediator greatly increases the specific capacity of the battery [1–7]. Among the many possible metal-air systems, the iron-steam battery provides very inexpensive, earth-abundant, and environmentally-benign battery materials [5,7–11]. Furthermore, this battery system can be paired with an industrial process with high waste heat (such as steel, glass or cement production, or even gas turbines) to maintain the high operating temperature (550–800 °C) required for the operation of iron-air batteries [12–15]. Practical configurations - including redox-flow batteries, encapsulated gas-flow batteries, air cathode materials design, and electrolyte design - are all active areas of research for iron-air batteries with particular focus on the evolution during cycling of the metal/oxide anode [6,8,14,16].

In this work, we consider our foams for a possible implementation similar to that described by Huang and coworkers [8,10] where the energy storage material was kept in a separate device to supply the solid-oxide fuel cell, functionally a reversible iron-air battery. The redox cycling of the energy storage material uses a fixed amount of H2O/H2, while O2 is supplied/released at the air electrode via ambient air flow. In this configuration, a steady supply of gasses is not be required, only some initial amount of H2O and ambient air are needed. Heating the system and designing components capable of functioning at high temperatures is a concern, however; either waste heat use or some parasitic load would be needed to raise and maintain the temperature, decreasing the efficiency of the system at high temperatures.

Metal-air systems often exhibit short lifetimes due to rapid degradation of the metallic anode during redox cycling, preventing their widespread adoption [1,3,5,17]. For iron-air batteries, degradation occurs by loss of available surface area in the anode due to the extreme volume change associated with the redox reactions. These reactions at high temperatures (> 550 °C) are shown in

* Corresponding author.
E-mail addresses: samuelpennell2024@u.northwestern.edu (S.M. Pennell), jacobmack2022@u.northwestern.edu (J.B. Mack), dunand@northwestern.edu (D.C. Dunand).
[1] These authors contributed equally to the presented work.

https://doi.org/10.1016/j.jallcom.2022.165606
0925-8388/

Equation 1, with the forward direction indicating battery discharge and the reverse direction indicating battery charge.

$$Fe + H_2O \leftrightarrow FeO + H_2 \quad (1a)$$

$$3FeO + H_2O \leftrightarrow Fe_3O_4 + H_2 \quad (1b)$$

The very large molar volume expansion on Fe oxidation (77 % increase for Fe to FeO, 110 % for Fe to Fe_3O_4) is the origin of the degradation during cycling [18]. Iron powder beds usually consist of packed Fe particles (0.1–20 μm in size) that are pressed and sintered [11,18]. In these beds, as neighboring Fe powders oxidize and expand, contact between powders increases [11,18–20]. At the high operating temperature, these contact points and the internal stresses from the constrained expansion induce sintering of the oxide powders; this causes a loss of open porosity in the powder bed which is not recovered upon reduction. This loss of porosity corresponds to a loss in available active material during practical charge or discharge times of ~ 1 h, due to the increased diffusion distance needed to react metallic iron with incoming steam.

To address this challenge, we have previously shown that freeze-casting Fe_2O_3 powders produces porous lamellar Fe_2O_3 foams, with thin, aligned lamellae providing the high surface area needed for operation, with slower degradation achieved by channels between lamellae, which provide gas access and reduce contact and sintering during oxidation [21–23]. The trade-off for this improved structural integrity is a larger volume (arising from the foam porosity) as well as slower reaction rates, since the anode morphology is planar rather than spherical and thus presents less surface area to the incoming gas. Directionally freeze-cast structures with lamellar channels provide easy paths for steam or hydrogen flow. These channels can be made sufficiently wide so that they do not choke gas flow (steam ingress and hydrogen escape) during the oxidation step, when the lamellae volume doubles [24,25]. However, this large volume change still results in instability in the lamellar architecture during cycling, i.e., pore formation within, and fracture and buckling of, lamellae causing sintering at lamellar contact points.

The main goal in choosing an alloying element for lamellar iron-air structures is to maintain the lamellar morphology for as many cycles as possible, thus allowing continued operation with high capacity and fast kinetics. This is accomplished by preventing various degradation mechanisms - lamellar buckling, plastic deformation, pore formation, or fracture - allowing each lamella to return to its original shape after reduction to its low-volume metallic phase. If lamellar fracture and buckling are not prevented, neighboring lamellae may contact in the oxidized state, resulting in (i) sintering at the area of contact (which occurs rapidly at the high temperature of operation), and (ii) internal mismatch stresses during reduction, eventually leading to densification of neighboring lamellae. This coarsening mechanism lowers the surface area available for subsequent redox reaction, thus lengthening reaction times, while also restricting gas flow if sintering shrinks the overall foam volume which lowers the channel open volume.

If no internal lamellar support is present when the Fe is fully oxidized, or if the structure cannot enable healing and the closing of lamellar pores, reduction in pure Fe foams usually results in each lamella splitting into two, as the stresses of rapid volume expansion drive crack propagation through the brittle oxide [22]. Though this is not ostensibly detrimental to surface area available for reaction, the split half-lamellae are more prone to buckling owing to their reduced cross-sectional area, so the foam sinters rapidly [22]. Another key microstructural change that hastens degradation is the formation of Kirkendall pores during oxidation; these pores widen lamellae, contributing to increased diffusion distances and decreased channel porosity [26].

Previous investigations have shown that the various mechanisms responsible for lamellar foam sintering during redox cycling can be mitigated by alloying Fe with 7–25 %Ni [26,27] (all compositions are given in at% in what follows). The Ni additions strengthen the lamellae during all stages of cycling. In the metallic state (at the start of oxidation or the end of reduction), the solid-solution strengthening provided by Ni helps reduce lamellar buckling. Once Fe oxidation is complete, an inert metallic Ni core (which does not oxidize under steam) prevents lamellar fracture by adhering to the Fe_3O_4 scale on the surface of the lamellae. Finally, Ni additions provide healing of Kirkendall micropores within lamellae via diffusion, if given a sufficient re-homogenization period [26].

Here, we investigate two new alloying additions in the Fe-steam battery, i.e., Co and Cu, and we examine microstructure, reaction kinetics, and bulk morphological evolution, under redox cycling, of lamellar Fe-Co and Fe-Cu foams. The relatively high testing temperature (800 °C) has an effect on the kinetics: reaction rates and diffusion will be faster, but the phases formed are identical for lower temperature (600 °C) operation [28,29]. We predict that our findings are relevant for lower temperature operation, although the cycle times and degradation observed here are accelerated as compared to a lower temperature. Different behaviors during redox cycling may be expected among the three types of foams, Fe-25Ni [26], Fe-25Co (present study) and Fe-30Cu (present study). First, we focus on the solubility of Co and Cu in Fe, at the operating temperature of 800 ºC, as shown in the phase diagrams in Supplementary Fig. 1: (i) Co and Fe show two phases, with extensive solubility for each other: fcc-Co-(0–17)Fe and bcc-Fe-(0–72)Co; (ii) Cu and Fe also show two phases, but with very little mutual solubility: fcc-Cu-(0–1)Fe and bcc-Fe-(0–1)Cu. Thus, the microstructures of the two types of freeze-cast and sintered lamellar foams, before cycling, are different: a single-phase Fe-25Co solid solution and a two-phase mixture of nearly pure Fe and Cu, respectively.

Second, we show that the oxidation pathways exhibit similarities, given that neither Co nor Cu form stable oxides with steam at 800 ºC, so that Fe is in all cases preferentially oxidized into a shell at the surface of the lamellae, rejecting Co and Cu into the lamellae center (as previously observed for Fe-25Ni foams [26]). Upon subsequent reduction, however, we find that the reduced Fe shell can re-homogenize with the Co-rich core (similarly to the Ni case [26]), but not with the Cu core, given the very different mutual solubilities in the Fe-Co and Fe-Cu systems. The re-homogenization of Co and Fe during reduction provides reversibility in the microstructures and delays foam densification, as also observed in Fe-Ni foams during re-homogenization of lamellae with Fe shells and Ni cores [26]. The lack of re-homogenization of Fe shells with Cu cores, however, exacerbates lamellar fracture and buckling, thus accelerating foam densification. Finally, we investigate the kinetics of redox reactions via *operando* X-ray diffraction. We show Cu additions more than double the rate of oxidation of Fe to Fe_3O_4, a significant increase over previously studied Fe and Fe-25Ni foams [26,27].

2. Experimental procedures

2.1. Freeze casting and sintering of foams

Lamellar mixed oxide foams were produced via directional freeze-casting, using the same procedures described previously in Ref. [26] for Fe-25Ni foams. Briefly, Fe_2O_3 powder (Noah Technologies, < 3 μm) and either CuO powder (SkySpring Nano, 99.9 %, 40 nm), Co_3O_4 powder (SkySpring Nano, 99.9 %, 50 nm), or NiO powder (Skyspring Nano, 99.9 %, 50 nm) were added to DI water to produce a slurry with 12 vol% solid oxides, with correct stoichiometry to form either pure Fe, Fe-25Ni, Fe-25Co, or Fe-30Cu (at%) when fully reduced. Zephrym PD 4974 (0.5 wt%) was added as a dispersant to the slurry which was mixed in a rotary ball mill with zirconia milling media (equal volume of media to slurry) for 48 h to reduce particle agglomeration. After milling, polyethylene glycol

(PEG, Mn~35,000, 1.4 wt%) was added as binder by dissolving in a volume of DI water calculated to account for losses during milling to produce a slurry with 10 vol% solid oxides and 2.5 vol% additives (balance H_2O). Finally, 4 M HNO_3 was added dropwise to the slurry to bring its pH to 6. The slurry was vacuum degassed before freeze casting and stored in an ice-water bath at 0 °C (with PEG preventing freezing) prior to casting.

Freeze casting was carried out in a cylindrical Teflon mold (15 mm ID, 26 mm OD, 15 mm height) placed on a copper plate and insulated with styrofoam. The copper plate was cooled by a thermoelectric cooling device (Mauser Technologies) to 0 °C before casting. After the 0 °C slurry had been poured into the mold, the suspension was cooled in an exponential cooling curve from 0 to −30 °C to ensure a constant freezing velocity of 16 µm/s [30]. Once fully solidified, the lowest 1 mm of the frozen sample was removed with a razor blade. The solidified samples were then freeze-dried for 48 h in a Labconco dryer at −22 °C and 0.13 mbar vacuum to ensure full ice sublimation before sintering. The dried green bodies were placed in an alumina tube furnace (42 mm ID, 50 mm OD, 700 mm length) and held at 300 °C for 1 h in flowing H_2 (99.999 % pure, Airgas) to burn out the binder and dispersant. In the same gas environment, they were then reduced at 600 °C for 4 h and sintered at 1000 °C for 3.5 h. Heating rate and cooling rate were 10 °C/min and 5 °C/min, respectively, for all steps. The reduction and sintering steps lead to shrinkage of the foams, similar for all 4 compositions: the diameter dropped from 15 to ~9 mm and height from 14 to ~6 mm, with some variations (typically ± 1 mm in either dimension) from sample to sample. This represents an average macroscopic shrinkage of 85 % from green body to metallic sample.

2.2. Redox cycling

For all four compositions, redox cycling was performed at 800 °C using alternative flows of H_2- and H_2O-rich gases in an alumina tube furnace (1.9 cm ID, 25 mm OD, 610 mm length). In this way, fewer cycles are needed to assess the damage resistance of a given alloy system. Initially, each metallic foam, positioned on an alumina plate, was raised to 800 °C at 10 °C/min under a 100 sccm flow of H_2 (99.999 % pure, Airgas). The 60-minute oxidation half-cycle was conducted under a 120 sccm flow of steam-saturated Ar, created by flowing Ar (99.999 % pure, Airgas) through a water bubbler held a 93 °C (to achieve a H_2O partial pressure of 0.77 atm). The subsequent 90-minute reduction half-cycle again used pure H_2 (200 sccm, partial pressure of 1 atm). These partial pressures were chosen to form Fe_3O_4 during oxidation and Fe during reduction [28,31]. After one or more such redox cycles, the samples were cooled at 10 °C/min under H_2 (100 sccm) when ending at the end of a reduction step. When ending during a partial oxidation or reduction half cycle, foams were instead cooled under Ar-4 %H_2 (20 sccm, Airgas) to minimize oxidation or reduction during cooling. Foams were measured and weighted before and after cycling, and mass change was used to confirm full conversion between Fe and Fe_3O_4 for the cycle times above.

Foams were vacuum-mounted in epoxy (Epothin 2, Buehler), ground on a rotating wheel to roughly halfway through the sample height, and polished via standard metallographic procedures, with the final step using a 1 µm diamond suspension. Foam radial cross-sections were optically imaged (Nikon Eclipse MA200, Wild M3Z Stereoscope), and ImageJ was used to derive microstructural parameters. An image of the entire radial cross section (perpendicular to the solidification direction), created by stitching low-magnification optical micrographs, was converted to binary pixels between metallic lamellae and epoxy background (channel volume). These slices were then processed by twice applying a median filter (radius of 3 pixels) to exclude micropores within lamellae. Channel porosity was then calculated by taking the ratio of the solid lamellar area to the total area within the outline of the foam. The ImageJ plugin "Local Thickness" was applied to the filtered image to calculate both lamellar wall thickness and channel thickness [32]. Previous tomography studies have confirmed that these measurements on 2D slices are representative of the bulk foam [22,33]. Imaging via scanning electron microscopy (SEM) and electron diffraction spectroscopy (EDS) was performed with a Hitachi 8030, under 15 kV accelerating voltage and 10 µA probe current, on mounted, polished foams which had been sputter-coated with 10 nm of Au-Pd alloy prior to imaging.

2.3. Operando X-ray diffraction (XRD)

For the Fe-25Co and Fe-30Cu foams, *operando* XRD data were collected on a Stadi-MP (Stoe, Germany) instrument, equipped with an asymmetric curved germanium monochromator under pure Ag-$K_{\alpha1}$ radiation ($\lambda = 0.5594$ Å) and a one-dimensional silicon strip detector (MYTHEN2 1k, from Dectris, Switzerland). The line-focused X-ray beam was operated at 40 kV and 40 mA (Beam Size 4 ×0.8 mm). Data were collected in Debye-Scherrer geometry, using 10-second scans for 2θ between 10.7 and 29.2º. A representative colony of lamellae was cut with a razor blade from the reduced, sintered foam, measuring 1 – 1.5 mm in height and width, and 0.5 mm in thickness, and introduced into a 1.5 mm ID glass capillary. Within the capillary, the sample was sandwiched by two layers of amorphous quartz wool, which were in turn abutted by ceramic spacers that extended the length of the capillary; these prevented sample movement while gas flowed through the capillary. Neither the quartz wool nor the ceramic spacer was within the X-ray beam, and they were chemically inert with the sample. The capillary was placed into a graphite-heated, water-cooled resistance furnace, allowing for rapid heating and cooling. Temperature stability was ~0.1 ºC. The sample was first heated at 30 ºC/min to 800 ºC under Ar-4 % H_2 and held at that temperature during subsequent redox cycling. For oxidation, Ar (99.999 % purity, Airgas) was bubbled at a 50 sccm rate through 93 ºC water, and the Ar-steam gas was then flowed into the capillary via heated Cu tubing to prevent steam condensation. For reduction, an Ar-4 % H_2 mixture was flowed at 50 sccm through the capillary, using dilute hydrogen to slow the reduction kinetics. The instrument was calibrated against a NIST Si standard (640d) prior to measurement.

Processing of diffraction data was done in Python following procedures described in Ref. [34]. 2D waterfall plots are derived using the Cmocean package [35]. To determine diffracted peak intensity and lattice parameter values, all spectra were first background-corrected using asymmetric least-squares smoothing [36]. Further smoothing was performed by binning the data, then taking the median of each bin. Individual peaks were then fit using the lmfit package, modeling Pseudo-Voigt profiles [37]. Integrated peak areas were calculated directly from the Pseudo-Voigt fit. Peak centers were directly converted to lattice parameter, and then converted to a relative change (expressed in %) in lattice parameter relative to the maximum lattice parameter observed for each phase throughout the experiment. To reduce noise in both peak area and lattice parameter data, binning is used; the scans were binned per 6 scans and the median value of the bin was taken as representative. The binned data were normalized to the highest median value. Both binned data and raw data are presented.

3. Results and discussion

3.1. XRD measurements of reaction kinetics

3.1.1. Fe-25Co foam

The XRD experimental setup required foam samples much smaller than the full foam used for macroscopic cycling, so gas composition was adjusted to slow the reaction and achieve good

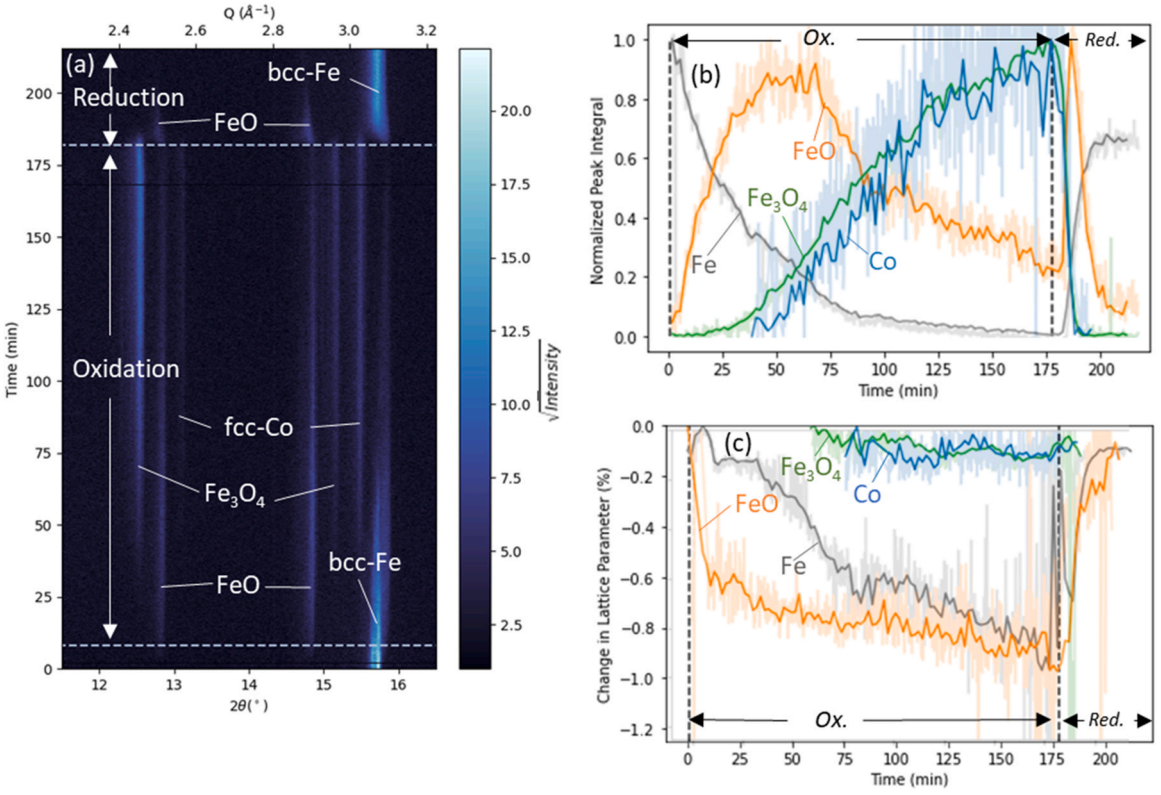

Fig. 1. Operando XRD results for Fe-25Co. (a) Time series of X-ray diffractograms showing the following reflections: (110) for bcc-Fe, (111) and (200) for fcc-Co, (111) and (200) for FeO, and (311) and (400) for Fe_3O_4; (b) evolution of normalized integrated peak intensities for the phase strongest peak (listed first in caption for (a) and marked on the diffractograms), and (c) evolution of normalized lattice parameters for the strongest peak of each phase. (b) and (c) show data that were binned over six scans and the median of each bin re-normalized then plotted to reduce noise. The raw data points (collected over 6 s intervals) are shown in the transparent overlay. The re-normalization of the binned data results in an offset for the Fe_3O_4 data, which contains high outliers before binning.

time resolution: a dilute Ar/4 % H_2 (instead of pure H_2) was used for reduction, and a lower flowrate of steam was used for oxidation. Thus, the reaction times for *operando* XRD are not directly comparable to those for bulk foam reactions, but they can be compared to other systems tested in the same XRD setup.

Fig. 1a shows XRD spectra cascade plots for the Fe-25Co foam, for a 225 min experiment, consisting of a first 10 min stabilization step under Ar, followed by a steam-oxidation step lasting 170 min and a hydrogen-reduction step lasting 45 min. Only part of the full spectra is shown, comprising the most intense set of reflections relevant to the Fe-Co system: bcc-Fe (110), fcc-Co (200) and (111), FeO (200) and (111), and Fe_3O_4 (311) and (400). Fig. 1(b–c) show, for the strongest peak corresponding to each phase, normalized peak integrals and normalized lattice parameters. *Ex situ* XRD tests at ambient temperature for 0 %, 30 %, 70 %, and 100 % oxidation and reduction were used to verify that the *operando* samples were representative of the reactions occurring in the bulk samples.

Fig. 1(a–b) show that the Fe-25Co foam begins as a single bcc Fe (Co) phase, consistent with the ternary phase diagram (Supplementary Fig. 1). At the onset of oxidation (t = 0 min in Fig. 1b), FeO forms immediately, reaching a plateau after 30 min. This plateau lasts ~45 min, as the rate of FeO formation (from Fe) is balanced by the rate of FeO conversion (to Fe_3O_4), which starts after an incubation time of ~30 min. At t = 45 min, 15 min after the start of Fe_3O_4 conversion, the newly formed fcc Co(Fe) phase becomes measurable, and grows at the same normalized rate as the Fe_3O_4 phase, up to the end of the cycle. This metallic phase corresponds initially to the Co-rich layer under the oxide scale of each lamella (discussed in detail below) and later becomes the Co-rich core when most of the Fe is oxidized and forms a Fe_3O_4 scale on each lamella. This Co-rich core contains a small amount of Fe (Co-1Fe, based on the phase diagram), but most of the initial Fe content is oxidized. The conversion from FeO to Fe_3O_4 continues until the end of the half cycle (t = 180 min), at an ever-diminishing rate, with significant amounts of FeO present at t = 180 min. The full oxidation pathway is shown in the Fe-Co-O ternary phase diagram in Supplementary Fig. 2, and the final metallic composition is estimated as Co-1Fe.

The oxidation rate of the Fe-25Co foam in Fig. 1b is slower (by a factor of 2) as compared to unalloyed Fe foam [29]. This can be explained by the more complex Fe-25Co oxidation sequence. The initial oxidation leaves a Co-rich layer at the interface of the newly formed oxide scale and the metal lamella. These regions and the further microstructural evolution of the sample are described in detail in a latter section. For further oxidation, Fe atoms must diffuse through this Co-rich layer (while Co atoms diffuse to the core), then the Fe must diffuse through the growing scale to the free surface; thus, overall oxidation reaction may change from surface-limited to a more sluggish diffusion-limited regime [38].

As reduction begins (t = 180 min), Fe_3O_4 and fcc-Co(Fe) simultaneously and quickly (within ~ 10 min) disappear, while metallic bcc-Fe forms rapidly. FeO briefly forms, peaking 5 min after reduction starts (t = 185 min), as an intermediate product for the reduction from Fe_3O_4 to Fe. After 20 min reduction (t = 200 min), the sample consists mostly of bcc-Fe(Co) with no fcc-Co(Fe), indicating that re-homogenization in the metallic phase is rapid. Comparison to previous experiments [39] with Fe foams indicates that the reduction is accelerated in the presence of Co, likely due to high activity of the Co core catalyzing the reduction reaction [26]. Some FeO remains present at the end of the experiment, probably due to encapsulated oxide phases that are cut off from gas access due to sample deformation induced from the stress of expansion and contraction, as shown in Supplementary Fig. 3.

Fig. 1a shows that, during reduction, the FeO main peak becomes sharper and shifts towards lower scattering vector Q values. Fig. 1c quantifies this shift by plotting the evolution of the FeO lattice parameter. This oxide is non-stoichiometric and can exhibit a broad composition range (from 51.25 to 52.6 at% O at 800 ºC): the initial $Fe_{0.92}O$ experiences a rapid drop (0.7 % in the first 10 min) in lattice parameter corresponding to the O-enrichment of the newly formed oxide. This drop levels off as FeO formation slows, with the small amount of FeO that remains at the end of oxidation having a lattice parameter 0.9 % lower than the initial value. During reduction, the reverse shift is observed as FeO becomes depleted in O and the lattice parameter rises. Also visible in Fig. 1c is that the lattice parameter of the bcc-Fe(Co) phase gradually drops during oxidation as the larger Co atoms leave the Fe lattice to form the fcc-Co(Fe) phase. That phase, on the other hand, shows almost no change in lattice parameter since it contains very little Fe content. During reduction, the bcc-Fe(Co) lattice parameter shifts rapidly back towards its initial value, increasing by ~0.5 %, as all Fe is reduced and dissolves into the Co core. This recovery of the original Fe(Co) lattice parameter is evidence that re-homogenization is occurring, recovering the initial, uniform Fe-25Co lamellar composition. This predicts a return to the initial state of the lamellae and has microstructural consequences that allow the foam to sustain redox cycling with little damage, as discussed further in later sections.

3.1.2. Fe-30Cu foam

Operando XRD data for the Fe-30Cu system are shown in Fig. 2(a–c), with the same reflections shown as for the Fe-25Co foam. Due to overlapping peaks between Fe_3O_4 (400) and Cu (111) under Ag-Kα radiation, the peak shifts occurring in Fe_3O_4 affect the Cu data. This is a non-physical data artifact (plotted in Supplementary Fig. 4, but omitted in Fig. 2(b,c)), as the peak intensity and lattice parameter of the Cu phase are not expected to change during cycling, given that Cu remains chemically inert during the redox cycle. Also, no Cu oxide (or Cu- and Fe- mixed oxide) is observed, as expected since Cu does not oxidize in steam at 800 ºC [40]. The peak broadening observed at the start of oxidation is a result of the coupling of relatively low counts (to preserve temporal resolution) and sample movement induced by the steam bubbler.

For Fe-30Cu (Fig. 2b), the oxidation of Fe follows a path similar to that observed in Fe-25Co: a first conversion of Fe to FeO is followed by a slower conversion to Fe_3O_4. However, since Cu, unlike Co, is insoluble in Fe, there is no emergence of a new metallic phase (similar to fcc-Co(Fe)). At the end of oxidation, the foam comprises only Fe_3O_4 and Cu (with ~1 % Fe in solid solution, based on the Cu-Fe phase diagram). The compositional path followed during oxidation is shown in the Fe-Cu-O ternary phase diagram in Supplementary Fig. 5. At the start of reduction (t = 70 min), most Fe_3O_4 is transformed to FeO within 3 min, as compared to 10 min for Fe-25Co. The reduction of FeO through its off-stoichiometric range is also visible in the shift of FeO peaks in Fig. 2b and by the lattice constant shift in Fig. 2c. After this shift is complete, FeO is reduced to Fe. After an initial rapid drop in FeO content, reduction rates slow, and significant unreacted FeO lenses are encapsulated within the foam at the end of the reduction half-cycle, due to sintering of the lamellae, as shown in Supplementary Fig. 6. These effects are exaggerated in the small sample volumes studied here, as compared to bulk foam samples, due to the lack of channel tortuosity in the sample slowing reaction rate, and the lack of an interconnected 3D lamellar network.

Though its channel architecture quickly disappears (as described in the later sections), the Fe-Cu system presents one clear advantage over the Fe-Co system: fast oxidation kinetics. *Operando* XRD captures the relative transformation of Fe to FeO and Fe_3O_4 during oxidation, and the reverse during reduction. These data show that

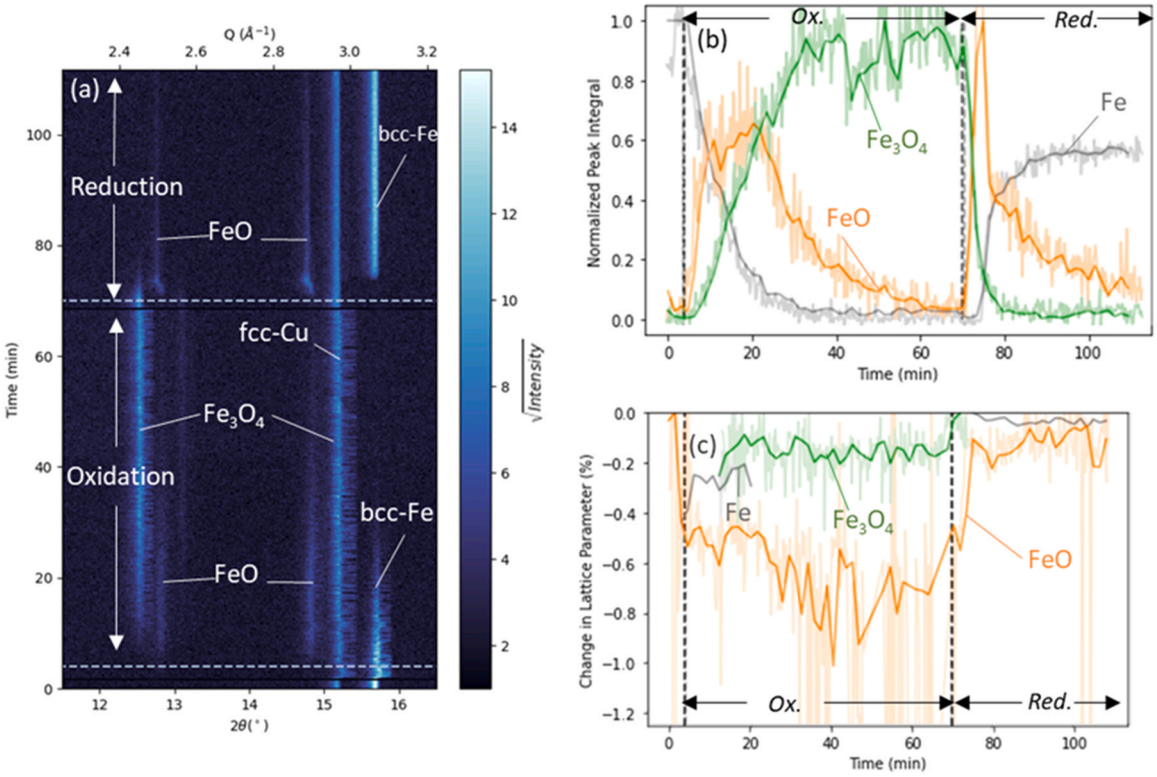

Fig. 2. Operando XRD results for Fe-30Cu. (a) Time series of X-ray diffractograms showing the following reflections: (110) for bcc-Fe, (111) and (200) for FeO, (111) for Cu, and (311) and (400) for Fe_3O_4; (b) evolution of normalized integrated peak intensities for the phase strongest peak (listed first in caption for (a) and marked on the diffractograms), and (c) evolution of normalized lattice parameters for the strongest peak corresponding to each phase present. (b) and (c) show data that were binned every six scans and the median of each bin re-normalized then plotted to reduce noise. The raw data are shown in the transparent overlay. The re-normalization of the binned data results in an offset for the Fe_3O_4 data, which contains high outliers before binning.

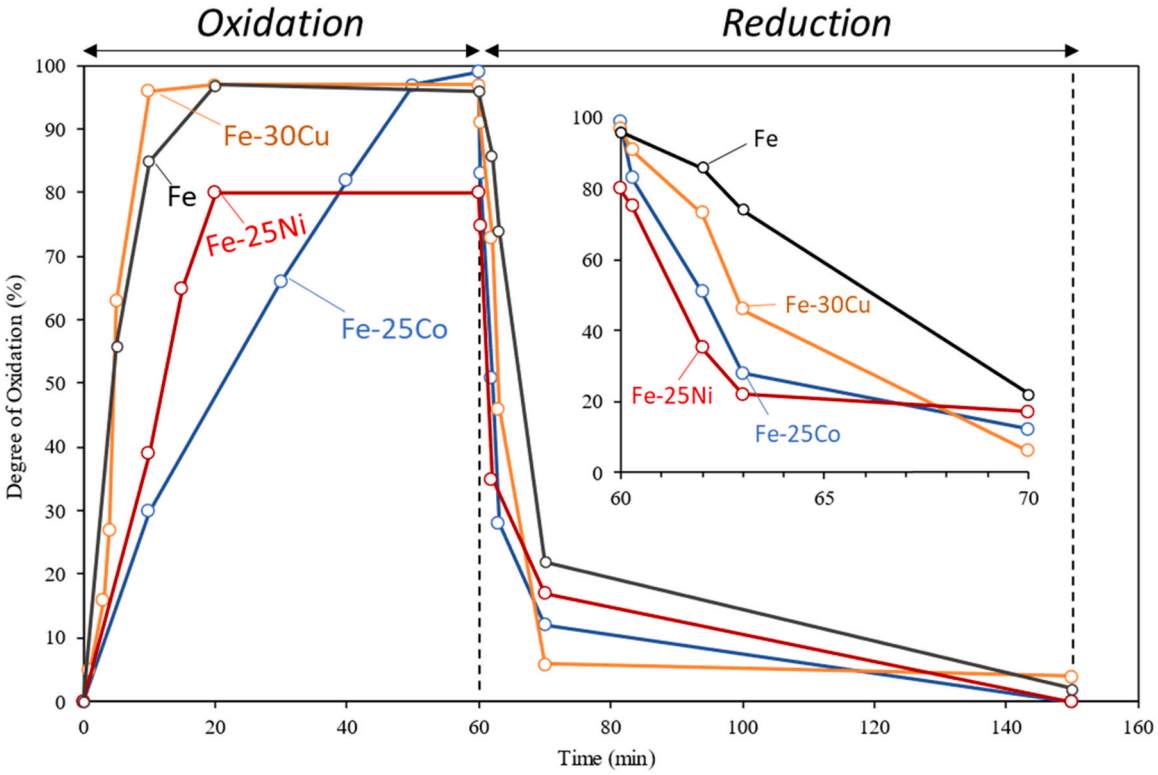

Fig. 3. Degree of oxidation calculated from mass gain (assuming conversion of Fe to Fe_3O_4) on individual sample of Fe, Fe-25Ni, Fe-30Cu, and Fe-25Co foams. Inset shows first 10 min of the reduction reaction.

the presence of Cu at the surface accelerates the oxidation reaction, leading to complete oxidation for an *operando* XRD sample after 42 min, as compared to 95 min for a pure Fe lamella, 140 min for a Fe-25Ni foam, and 175 min for a Fe-25Co foam [29]. This result is confirmed in cycling of bulk foams, where oxidation and reduction rates are measured by mass change, as shown in Fig. 3: the Fe-30Cu foam is 97 % oxidized after only 10 min of steam exposure at 800 °C, as compared to 39 % for Fe-25Ni [29] and 30 % for Fe-25Co. On H_2 exposure, reduction of the Fe-30Cu foam is 93 % complete after 10 min of steam exposure at 800 °C, as compared to 88 % for Fe-25Ni and 75 % for Fe-25Co. These enhanced rates of oxidation and reduction in the Fe-Cu foam present an opportunity for fast redox cycling.

We hypothesize that the Cu effect on Fe oxidation kinetics has both a chemical and a microstructural component. The chemical catalytic effect of Cu on the water-splitting reaction has been explored previously, and though monometallic Cu is considered a poor catalyst overall [41–43], some benefits have been observed in the Fe-Cu system [42]. The microstructural contribution towards the kinetic effect observed is due to the additional interfaces present within Fe lamellae due to Cu particles. These interfaces provide oxidation sites throughout the volume of the lamella, reducing the diffusion distance needed for Fe atoms to traverse in order to oxidize with H_2O.

3.2. Microstructure and microporosity

3.2.1. Fe-25Co foams

The microstructural evolution associated with redox cycling is shown schematically in Fig. 4 as a reference for discussion in this section.

Fig. 5 shows SEM images with accompanying EDS maps of representative Fe-25Co lamellae during the first redox half cycle, after 0 %, 30 %, 70 %, and 100 % oxidation as measured by mass change (assuming full conversion of Fe to Fe_3O_4, the equilibrium phase of iron-oxide present with steam [29,44]). For 0% oxidation, before redox cycling, the Fe-25Co lamellae appear densified after sintering following freeze-casting (some O signal is detected in all samples due to the oxygen content of the mounting epoxy). Steam initially oxidizes each lamellar exterior surface forming a thin oxide scale on each lamella (Fig. 5a, 30 % oxidation). Within a few minutes of steam exposure (Fig. 5b, 70 % oxidation), oxide veins appear within the lamellar interior (yellow arrows). These veins appear oriented perpendicular to the direction of lamellar growth, consistent with a connection to the lamellar surface. This implies that the lamellae - in the as-fabricated foams after the original reduction and sintering steps following the freeze casting - contain a network of fine channels connected to the lamella surfaces. These are expected to represent steam exit microchannels which were not fully sintered after the original reduction step and which are then oxidized rapidly with steam during the first redox cycle. These micron-scale oxide veins observed in cross-sections make up an interconnected, three-dimensional oxide network whose cross-section expands during oxidation, explored further by Mack et al. [39]. On the lamellae surface, the oxide scale grows as well, reaching a thickness of 3 µm after 60 min oxidation (Fig. 5c, 100 % oxidation).

A narrow, Co-enriched metallic layer is present under the oxide scale of each lamella (Figs. 4c, 5a, pink arrow), consistent with Co rejection from the growing Fe_3O_4 scale into the metallic core, as Fe is preferentially oxidized by steam. This layer, as it becomes Co-richer and thus less oxidation-prone with its continuing growth, is expected to slow the oxidation reaction as compared to Fe-30Cu or pure Fe: the inward diffusion of Co (driven by the concentration gradient with the Fe-rich core) and the continuing rejection of Co (as the Fe_3O_4 scale grows) result in the formation of a metallic core (Figs. 4d,5b–c, green arrows) which becomes gradually richer in Co and poorer in Fe, as oxidation proceeds. When sufficiently Co-rich, the alloy transforms from its original bcc-Fe(Co) to fcc-Co(Fe), as confirmed by XRD observations discussed above. The emergence of

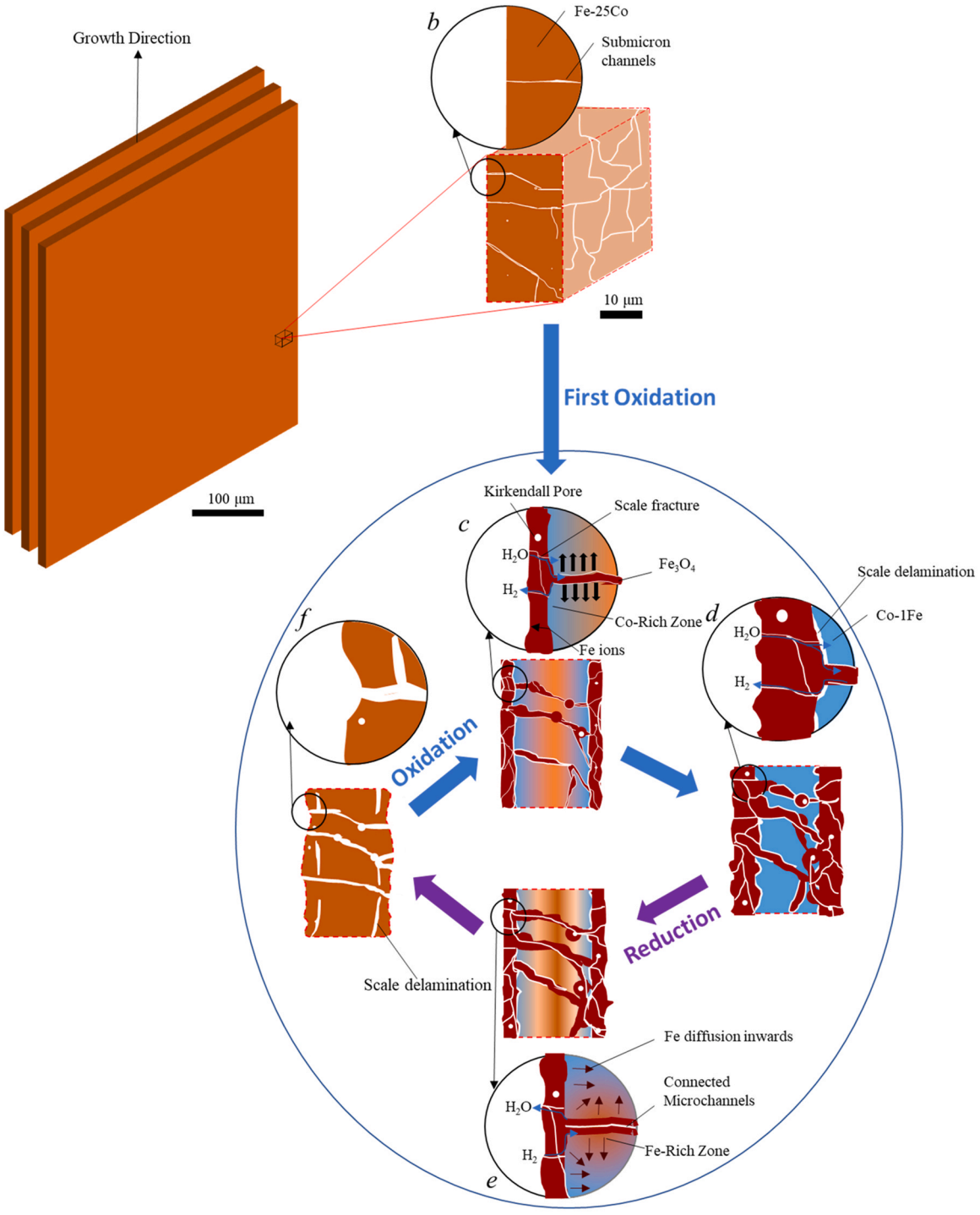

Fig. 4. Schematic illustrating the microstructural evolution during redox cycling of part of a single lamella, viewed in cross-section along the growth direction. Panel (a) shows a simplified 3-dimensional view of a lamellar colony, with a representative sample volume indicated in black. A magnified view of this volume and its evolution are shown in the following panels: (b) a fully homogeneous, as-fabricated Fe-25Co lamella with submicron-wide channels (from hydrogen ingress and steam escape during oxide reduction after freeze-casting); (c) partially oxidized lamella, showing oxidation at lamellar surface and in microchannels. The newly formed oxide scale develops infrequent Kirkendall micropores, and the diffusion of Fe to the oxidizing outer surfaces results in a gradient in Fe concentration from the core of the lamella to its outer surfaces; (d) fully oxidized lamella, with thick (~5 μm) scale forming a shell surrounding a Co core (with a small amount of remnant Fe in solid solution), intercrossed with oxide-filled microchannels, (e) partially-reduced lamella, with oxide reduction occurring at the interface between metal and oxide (both oxide scale and oxide microchannels). The volume contraction associated with Fe_3O_4 reduction cracks the oxide (containing previously formed Kirkendall pores) in the microchannels. Fe-rich regions close to the receding oxide scale are formed. Scale delamination is prevalent, resulting in additional cracks. (f) fully reduced lamella with fully homogenized Fe and Co concentrations and interconnected microchannels. Microchannels aligned with the direction of the concentration gradient allow for short-circuit diffusion, while cracks oriented perpendicular to this gradient (formed due to scale delamination) slow diffusion by increasing the diffusion path length. Schematic adapted from similar depiction of microchannels in Fe-25Ni lamellae in Ref. [39].

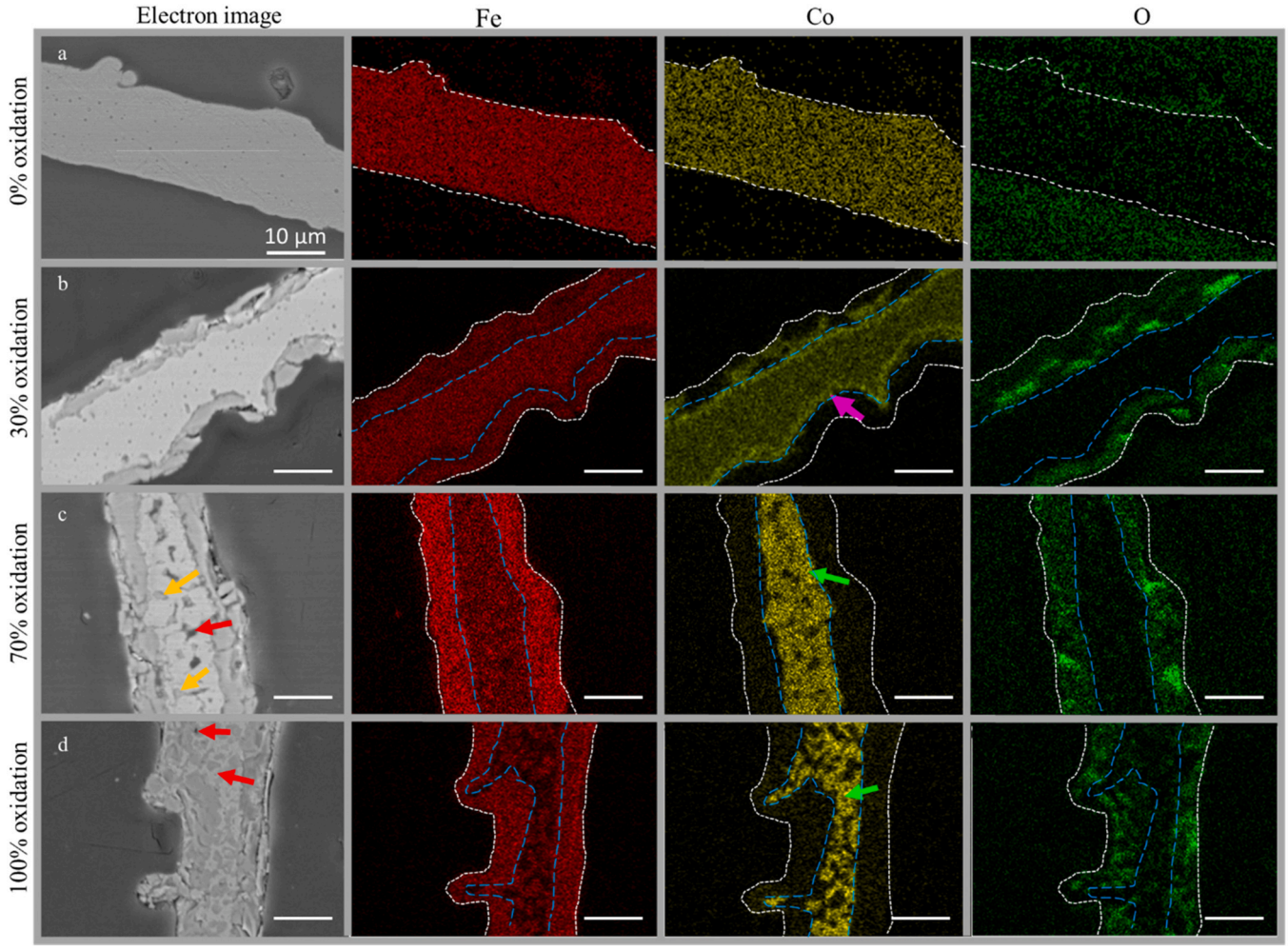

Fig. 5. SEM micrographs of representative Fe-25Co lamella cross-sections, with corresponding EDS maps for Fe, Co, and O, for foams oxidized (first cycle) to (a) 0 % (0 min), (b) 30 % (10 min), (c) 70 % (20 min), and (d) 100 % (60 min). White dashed lines mark surface oxide scale, blue dashed lines mark the interface between oxide scale and metallic core. Red arrows mark microchannel porosity, yellow arrows mark interior oxide veins, green arrows mark the Co-rich core, and pink arrows mark the Co-enriched layer forming at the onset of oxidation due to Co rejection from the oxide scale.

this new phase stands in contrast to the behavior of Fe-25Ni foams, which maintain a continuous Fe-Ni solid solution phase which becomes continuously Ni-richer as Fe is depleted by oxide formation [26]. Based on the trajectory in the phase diagram shown in Supplementary Fig. 2, no Co oxide or distinct mixed oxides are expected to form for steam oxidation of Fe-25Co; some substitution of Co atoms for Fe atoms in Fe_3O_4 might be expected, especially near the metallic core [45].

Although a network of microchannels is present within the Fe-25Co lamellae after initial sintering on foam fabrication, the lamellae exhibit very few Kirkendall pores in their metallic core upon full oxidation, unlike pure Fe and Fe-25Ni foams [26,27] (and Fe-30Cu foams, as discussed below). Kirkendall pores in those systems form due to the faster outward flux of Fe atoms through the oxide scale to the lamellar surfaces, as compared to slower inward flux of O atoms. It is hypothesized that the inward diffusion of Co to the metallic core, as oxidation proceeds, compensates the flux imbalance sufficiently to mitigates the Kirkendall effect. Some coarsened Kirkendall pores are observed in cross-section, but they are uncommon (Fig. 5b–c, red arrows).

Fig. 6 shows SEM micrographs and corresponding EDS maps during the first reduction half cycle, after 20 s (20 % reduced), 3 min (75 %) and 30 min (100 %) H_2 exposure, and after a re-homogenization period lasting an additional 60 min (for a total of 90 min). Reduction begins at the metal-oxide interface where the reaction is likely catalyzed by the Co-rich core, as also observed in the Ni-rich core of Fe-Ni foams [26]. Fe_3O_4 reduction occurs quickly as compared to pure Fe foams [39], and all oxide is reduced within 30 min, as measured by mass. The fine Fe_3O_4 network within each lamella appears to be reduced first (Figs. 4e, 6a), owing to the high interfacial area in contact with metallic Co. Because the H_2 was able to escape when these veins formed during the oxidation half cycle, these veins are expected to be gas accessible and can quickly reduce when H_2 is introduced during reduction. Further evidence for this mechanism is the formation of Fe-rich regions within the Co-rich core (Fig. 6b, yellow arrow), observed in numerous instances and shown schematically by the composition gradients illustrated in Fig. 4c–e.

During reduction, elongated microporosity forms within the lamellae as the oxide vein network becomes hollow (Fig. 5(a–d), red arrows) due to the 110 % volume change from Fe_3O_4 to Fe (Eq. 2). Due to the morphology of the Co-rich core in the fully oxidized state, when the oxide begins reducing at this tortuous interface, irregular pores are created where oxide veins were present. Porosity formation also causes the oxide surface scale to partially delaminate from the metallic core (Fig. 5a, violet arrow), an effect that is attributed to low Fe content in the Co-rich core leading to poor adhesion between the Co-rich core and the oxide: Fe has been shown to have higher adhesion strength to oxide [46]. This delamination upon the onset of reduction is less extensive in Fe-Ni foams, owing to the Fe-Ni solid solution present at equilibrium for full oxidation of these foams that likely better adheres to Fe_3O_4 due to its higher Fe content [26].

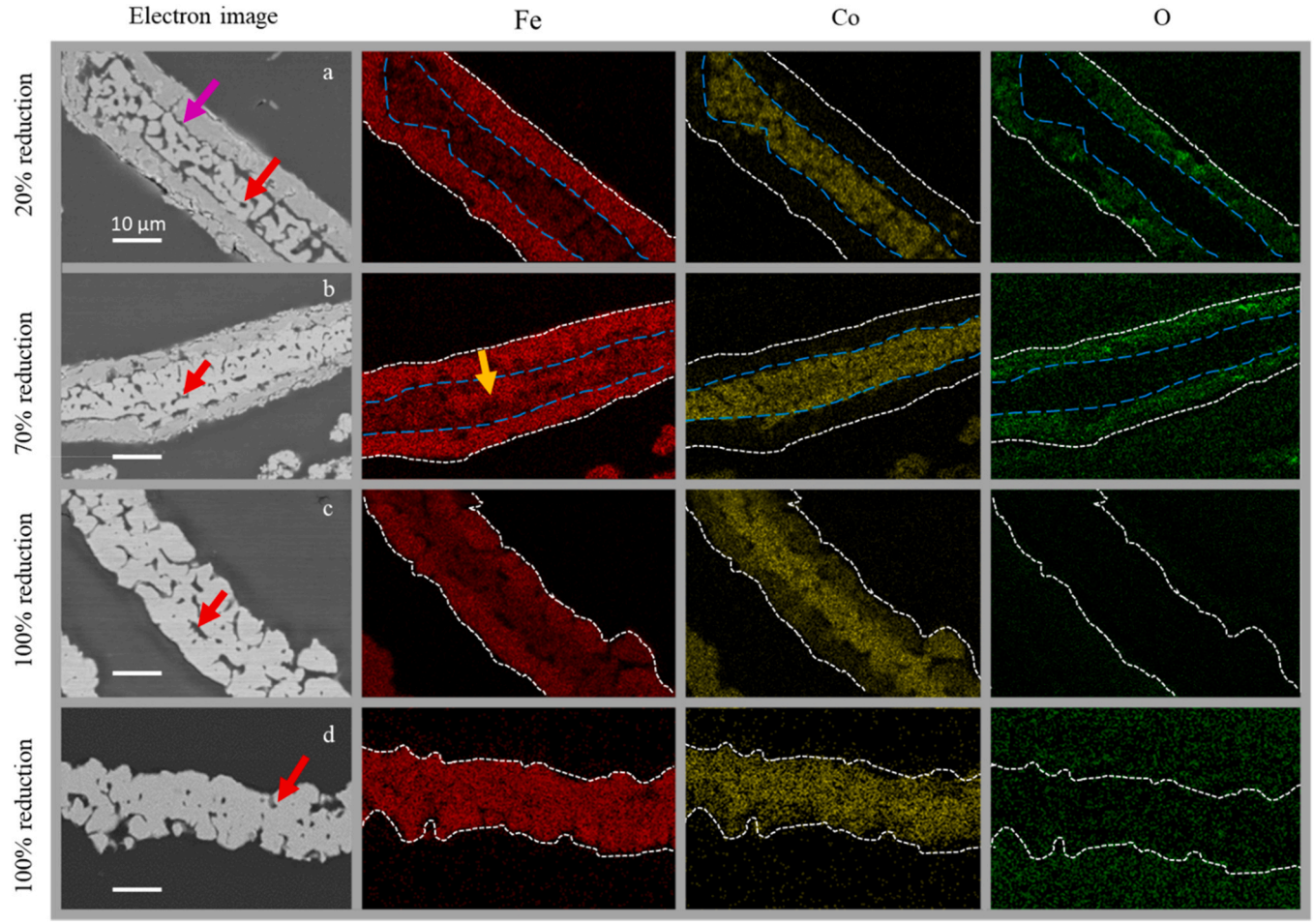

Fig. 6. SEM micrographs of representative Fe-25Co lamella radial cross-sections, with corresponding EDS maps for Fe, Co, and O, for samples reduced (first cycle) to (a) 20 % (20 s), (b) 70 % (3 min), (c) 100 % (30 min). The microstructure after the re-homogenization period of 90 min is shown in (d). White dashed lines mark surface oxide scale and blue dashed lines mark the interface between oxide scale and metallic core. Red arrows mark microchannels, the yellow arrow marks an interior Fe-rich core, and the violet arrow marks delamination cracks between the metallic core and the oxide scale.

The remainder of the cycling time (from 30 to 90 min) is dedicated to re-homogenization and porosity healing: the relatively high diffusion coefficient of Co in Fe (1.5×10^{-13} cm^2/s, 2.5 times higher that of Ni in Fe, 6×10^{-14} cm^2/s [47] at 800 ºC) allows each lamella to return to its initial, homogenous Fe-25Co composition, while also partially sintering the Kirkendall micropores created during reduction. In this period, it is likely that the microchannel network serves as an additional diffusion pathway by enabling surface diffusion within the lamella. The presence of a short-circuit diffusion mechanism other than bulk diffusion is inferred from the relatively long interdiffusion distance (~5 µm) needed to fully re-homogenize the sample, which is much longer than the characteristic bulk diffusion distance of just 0.2 µm for a 90 min period.

The cracks formed due to scale delamination, however, can have the opposite effect. Since they lie normal to the concentration gradient between the reduced Fe shell and the Co core, these cracks do not provide diffusional contact between the two regions. Instead, they lengthen diffusion distance locally, resulting in some Fe-Co heterogeneity that cannot be removed in the cycling time. This effect is more severe in the Fe-25Co system as compared to Fe-25Ni, as Co has, in general, lower adhesion to oxide scale than Ni or Fe [46].

An important effect of the formation of a Co-rich core within lamellae during oxidation is stabilization of the initial lamellar architecture through fracture prevention during oxidation and re-homogenization during reduction. Fracture is prevented by two mechanisms: (i) the Co-rich core adheres to the adjacent Fe_3O_4 lamellae and (ii) Kirkendall pores are prevented from growing and coarsening via fast Co diffusion which allows for more healing to occur during the re-homogenization period. This returns the microstructure close to its initial state before the next redox cycle occurs.

3.2.2. *Fe-30Cu foams*

A schematic depiction of the microstructural evolution of Fe-30Cu is shown in Fig. 7.

Fig. 8 shows SEM micrographs of representative Fe-30Cu lamella cross sections during oxidation. The foam Cu concentration (30 %, higher than 25 % Co in the Fe-25Co foams) was chosen to achieve a Cu volume fraction well above the percolation limit. The initial state of the Fe-30Cu microstructure is significantly different from that of Fe-25Co. As Cu has near-zero solubility in Fe, the Cu phase thus remains distinct from the Fe matrix (Figs. 7a, 8a). This phase separation, which is present at the surface as well (Supplementary Fig. 7), also impacts the evolution of the Fe phase oxidation: as each lamella begins as a fine, interpenetrating two-phase structure (Fe + Cu), instead of a solid solution (Fe-25Co); a Cu-rich solid-solution core does not initially form. Instead, as Cu is rejected towards the lamellar core as oxidation proceeds, the Cu phase coarsens within the Fe-rich phase, which is being consumed by oxidation. Bulk oxidation proceeds from the outside of each lamella inwards (along with oxidation along the nanometric channels formed during the initial sinter), engulfing the inert Cu phase, until all Fe is oxidized.

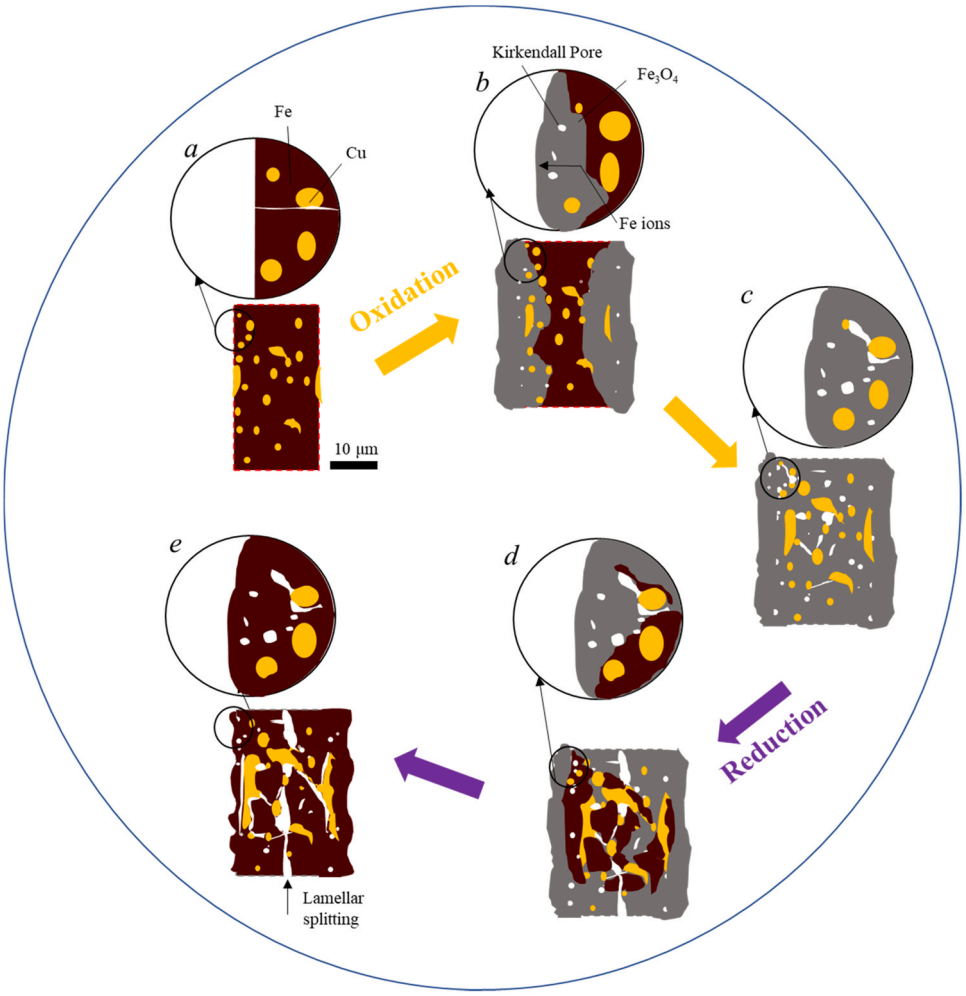

Fig. 7. Schematic depiction of microstructural evolution of Fe-30Cu during redox cycling. The initial fully metallic lamella, as-fabricated from reduction after freeze-casting, is shown in (a). Each lamella consists of an Fe matrix containing micro-sized Cu inclusions, resulting in a two-phase microstructure. The gas microchannels are again present, as in Fe-25Co. In (b), oxide scale growth proceeds inwards into the lamella, accelerated by the Cu at the surface as well as the increased interfacial area from the two-phase structure. Kirkendall pores are prevalent, as seen in pure Fe foams [27]. In (c) the fully oxidized lamella is shown; the Cu domains are segregated towards the lamellar core due to the expansion of the Fe_2O_3 scale during oxidation. Kirkendall pores have coarsened significantly, and those located near Cu domains can provide a surface diffusion pathway that enables Cu coarsening. Reduction begins in (d) at the Cu-oxide interfaces. Since there is no cohesive metallic core, lamellar splitting (arrow) is observed, as for pure Fe foams [27]. After reduction is complete, as shown in (e), the Cu phase has coarsened significantly. Cracks have formed along Cu-Fe interfaces, widening the lamella as compared to its initial state.

The oxidation of the Fe-30Cu samples proceeds faster than that of Fe-25Co, lessening the impact of the nanometric channels.

This mostly radial oxidation within each lamella is accompanied by the formation of significant Kirkendall porosity in the oxide layers (Figs. 7b, 8(b–c, red arrows). These pores form due to diffusivity mismatch between O and Fe atoms during oxidation, as previously reported in pure Fe foams [26]. Once nucleated, they grow and coarsen to occupy a significant volume fraction within the oxidized lamellae and lead to extensive deformation during reduction, as discussed below. However, these pores do not coalesce along the center plane of each lamella, as they do in pure Fe foams, due to the presence of a well-dispersed Cu phase (expected to form a continuous network in 3D) [27]. At the end of oxidation, the lamellae consist of coarsened Cu regions embedded within a Fe_3O_4 phase (fully converted from Fe), which in turn contains Kirkendall pores. Because Cu is insoluble in Fe (unlike Co or Ni) and cannot be rejected into the Fe-rich lamellar cores upon oxidation, a cohesive Cu-rich core does not form after the first cycle.

Fig. 9 shows representative lamella cross-section micrographs during the first reduction half-cycle, which occurs without a dense metallic core, unlike Fe-25Co foams. Reduction begins at the interface between the oxide matrix and the Cu phase, as also observed in the Fe-25Co lamellae. The large volumetric shrinkage during reduction results in fracture and microchannel formation as oxide in the vicinity of each Cu particle shrinks. These microchannels then may coalesce with the already existing Kirkendall micropores. The initial oxide scale is thick enough that some reduction also occurs at the outside of each lamella, as also observed in the pure Fe system [27]. Additional cracks form due to delamination at the Cu interface. This is expected since metallic Cu has relatively poor scale adhesion as compared to other transition metals [46]. The combination of these mechanisms, after all iron oxide is reduced, leads to elongated pores as seen in Figs. 9c and 7(d–e). They have, on average, an area of 20 μm^2, much above the value of 4 μm^2 for Fe-25Co. The continued exposure to H_2 does not heal these elongated pores in the Fe-Cu system since no rehomogenization can occur, but it provides time for the Cu phase to coarsen in the center of each lamella (Figs. 9d, 7e).

3.3. Evolution of macro- and microstructure during cycling

3.3.1. Fe-25Co foams

Fig. 10 shows low- and high-magnification images of Fe-25Co foam cross-sections after 1, 3, 5, and 10 redox cycles, illustrating the

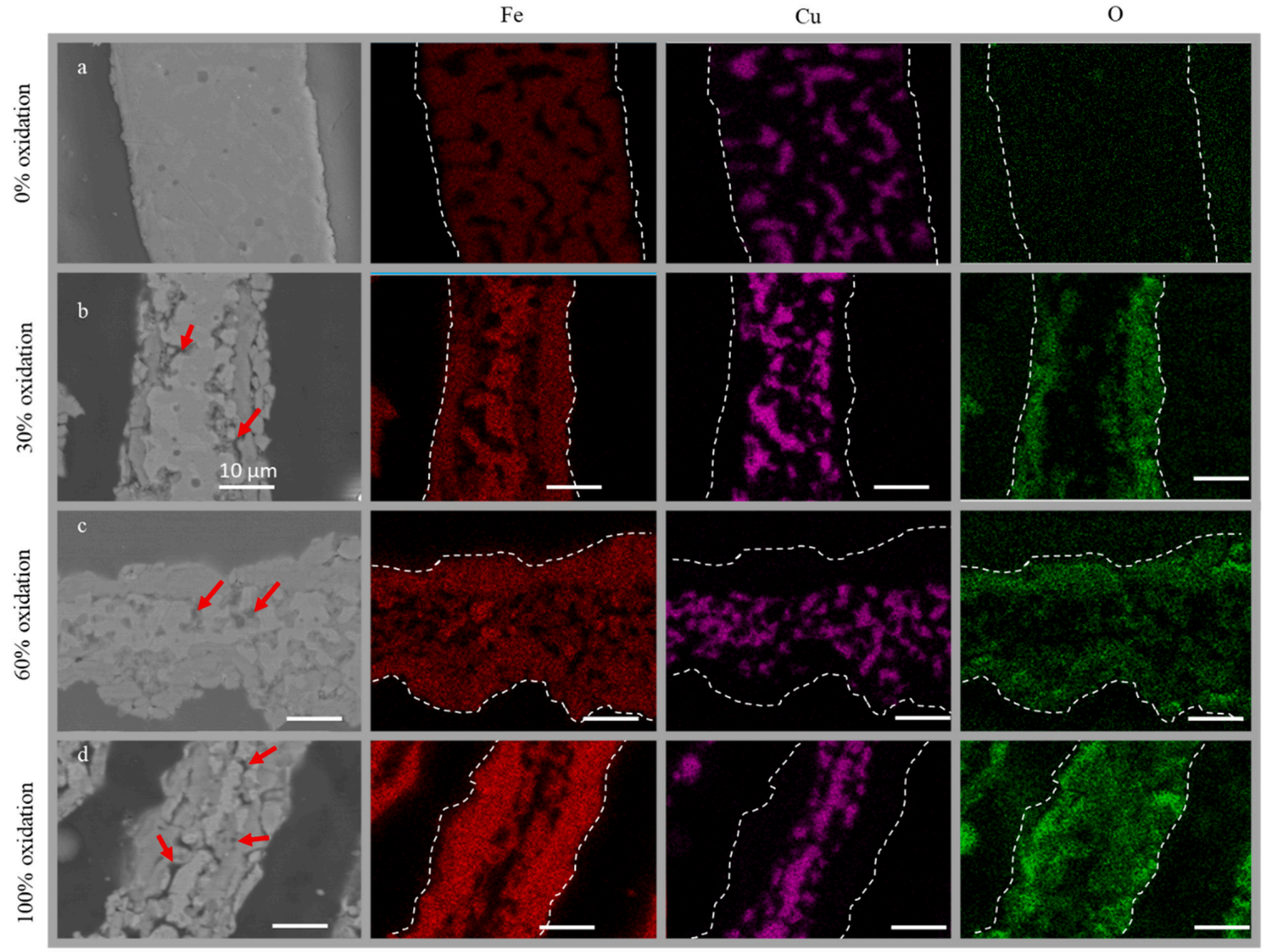

Fig. 8. SEM micrographs and corresponding EDS maps showing representative Fe-30Cu lamella radial cross-sections after oxidation (first cycle) to (a) 0 % (0 min), (b) 30 % (3 min), (c) 60 % (5 min), (d) 100 % (20 min). Red arrows in (b–d) mark Kirkendall pores.

foam macrostructure over a full cross-section and the corresponding lamellar microstructure. Some lamellar buckling occurs, but the Co-rich cores prevent lamellae from splitting (as they do in the pure Fe system [27]) and the re-homogenization period enables partial healing of the microporosity created in lamellae during each redox cycle. After the first cycle, the growth of additional microporosity is slower than the sintering of micropores that occurs during each successive re-homogenization period, leading to denser lamellae after multiple cycles (Fig. 10 d,e,f). Overall, the lamellar microstructure does not deteriorate over the first 10 redox cycles, enabling a stable foam macrostructure, with limited overall foam sintering (i.e., decrease in foam cross-section).

Despite the stability of individual Fe-25Co lamellae, there is evidence of lamellar sintering upon multiple cycles (Fig. 10, red arrows) in regions where lamellae contact and sinter during oxidation. Control experiments carried out under inert atmosphere without redox cycling show that these foams do not shrink upon sintering at 800 °C for 26 h (the same duration as 10 cycles). Thus, the volumetric sintering observed upon redox cycling is not due to prolonged high-temperature exposure; rather, it stems from buckling of the high aspect-ratio lamellae, driven by the volumetric expansion of the oxide upon oxidation. As lamellae are pinned at their edges within their colonies, as confirmed by previous 3D reconstruction studies, their planar expansion on oxidation is constrained, thus causing buckling [33]. Buckling in the present Fe-25Co foams appears more severe, with a more rapid onset, as compared to Fe-25Ni foams over the same number of cycles [26]. This is likely due to the composition of the core present upon oxidation: the Fe-Ni foam cores comprise a concentrated solid solution (fcc-Fe-Ni) instead of relatively pure, and thus weaker, fcc-Co(Fe).

3.3.2. *Fe-30Cu foams*

Fig. 11 shows corresponding low- and high-magnification images for Fe-30Cu foams after 1, 3 and 5 redox cycles. Since the foam fully densified after 5 cycles, further testing to 10 cycles was not performed. The key differences in microstructure as compared to Fe-25Co foams (Fig. 10) - lack of a cohesive lamellar metallic core and lack of Kirkendall pore sintering in the lamellae - have a profound effect on the macroscopic foam evolution. After 1 cycle, all lamellae develop significant Kirkendall microporosity in their center, greatly increasing lamellar contact on successive cycling due to increases in lamellar width. Significant lamella-to-lamella contact, and thus loss of interlamellar channels, are visible after the third redox cycle, and densification becomes near complete after the fifth cycle, albeit with microporosity present throughout the sample. The loss of distinct lamellae and channels drastically reduces foam gas permeability, making the binary Fe-30Cu system unsuitable for extended redox cycling.

The evolution of the macro- and microstructures for the Fe-25Co and Fe-30Cu foams is quantified through measurements of channel

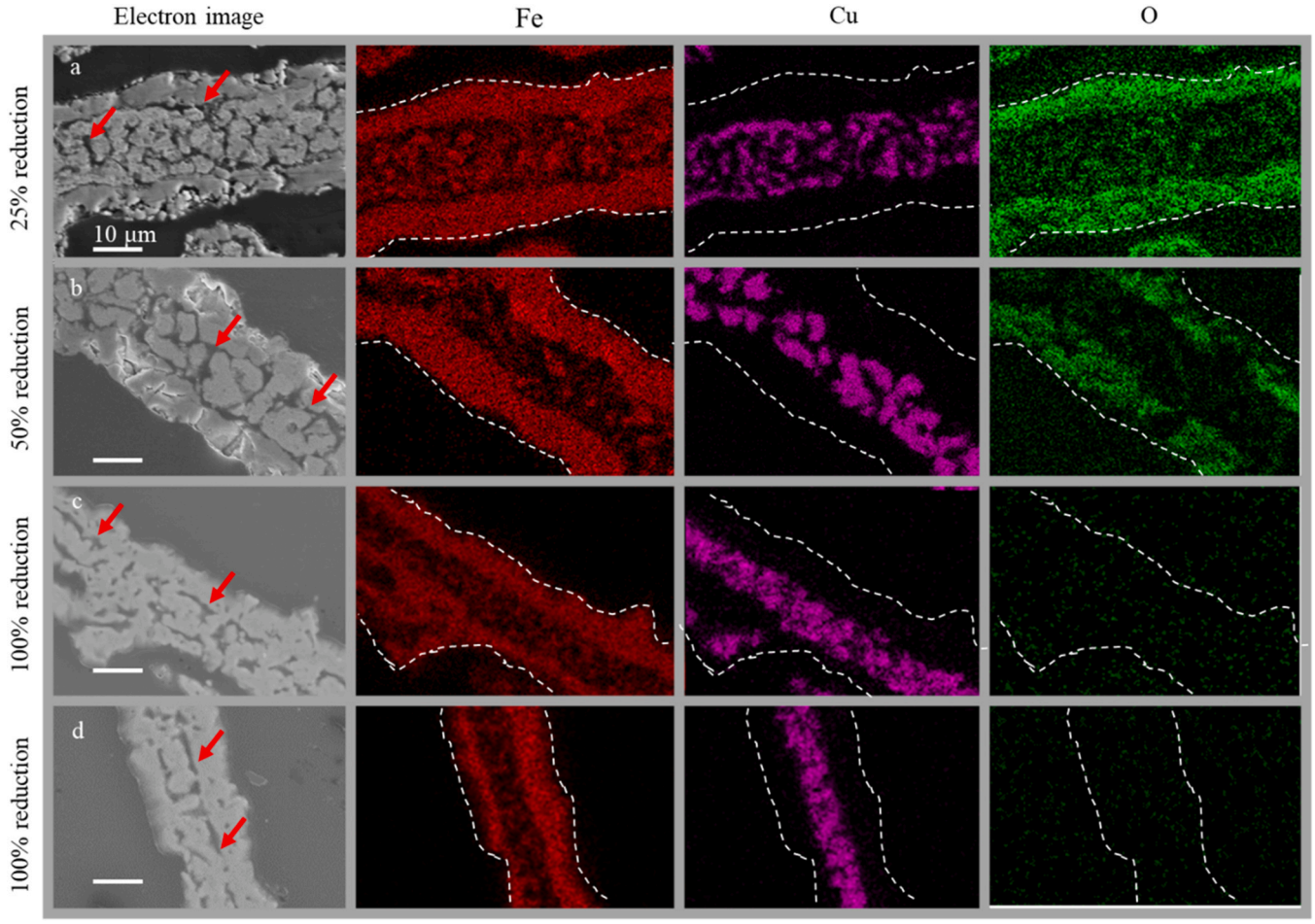

Fig. 9. SEM micrographs and corresponding EDS maps showing representative Fe-30Cu lamella cross-sections after reduction (first cycle) to (a) 25 % (2 min), (b) 50 % (3 min), (c) 100 % (10 min), and (d) 90-minute exposure to H_2. Red arrows point to elongated pores.

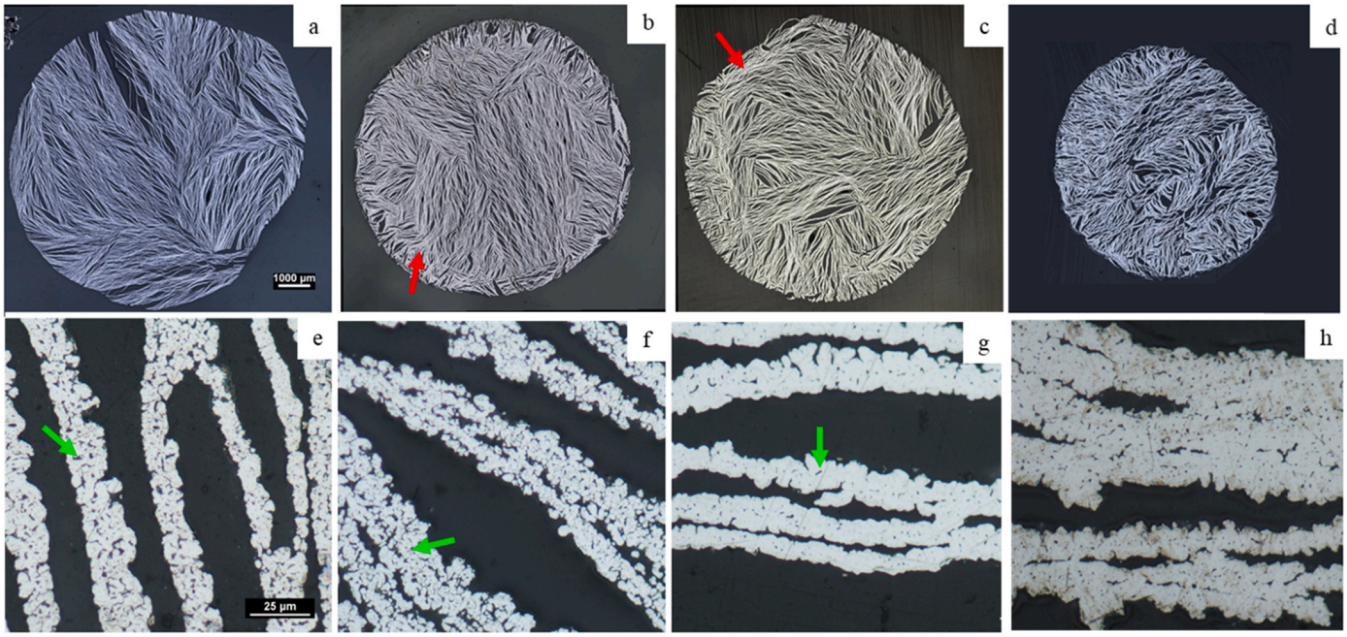

Fig. 10. Optical micrographs showing full cross-sections of foam (top row) and representative microstructure (bottom row) for Fe-25Co after redox cycling (a,d) 1 cycle (b,e) 3 cycles and (c,f) 5 cycles. Red arrows mark sintering in regions near the sample edge and green arrows mark microporosity within lamellae, which sinters as the number of cycles increases.

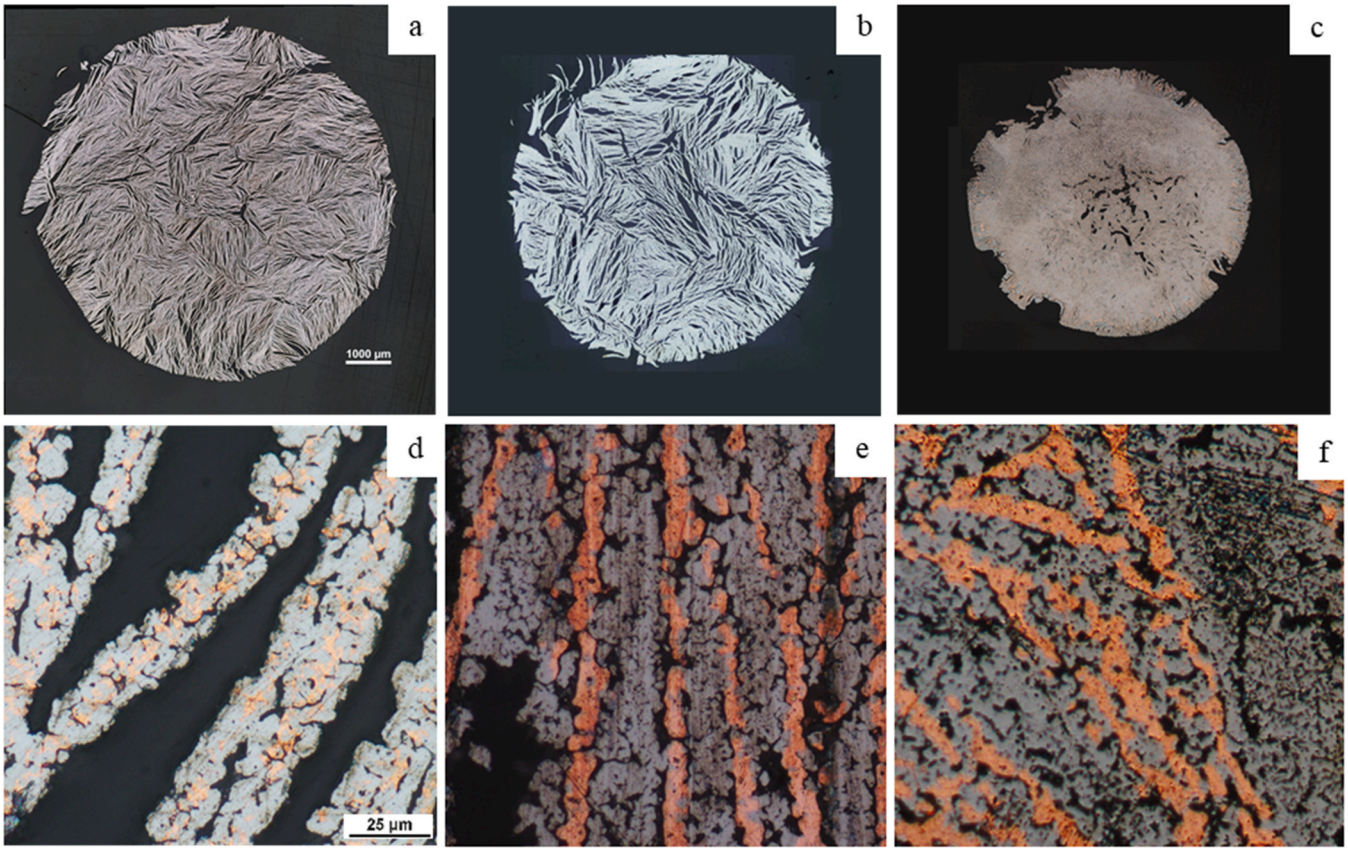

Fig. 11. Optical micrographs showing the macrostructure (top) and representative microstructure (bottom) for Fe-30Cu after (a,d) 1 redox cycle (b,e) 3 cycles and (c,f) 5 cycles, with Cu showing an orange color, and Fe a gray color. The progressive densification of the porous lamellar structure is apparent after 3 cycles, and the originally lamellar foam is almost entirely densified after 5 cycles.

porosity, lamellar thickness, and channel thickness, reported in Fig. 12. A stable foam should maintain high channel porosity for gas flow (i.e., little channel shrinkage), low lamellar thickness (i.e., no accumulation of Kirkendall micropores and no microcracking), and high channel thickness (i.e., no merging/sintering of neighboring lamellae), comparable to the as-cast foam structure. With repeated cycling, as lamellae deform (via buckling, Kirkendall swelling and internal delamination)such that they contact each other and sinter at contact points, so that channel porosity decreases. Here, Kirkendall micropores are not measured and not added to the channel porosity values, which describe the channel volume fraction.

Fig. 12 shows that, as expected from qualitative micrograph observations (Fig. 11), the channel porosity of the Fe-30Cu foams decreases rapidly with cycling, from 65 % to 9 % after 5 cycles. The

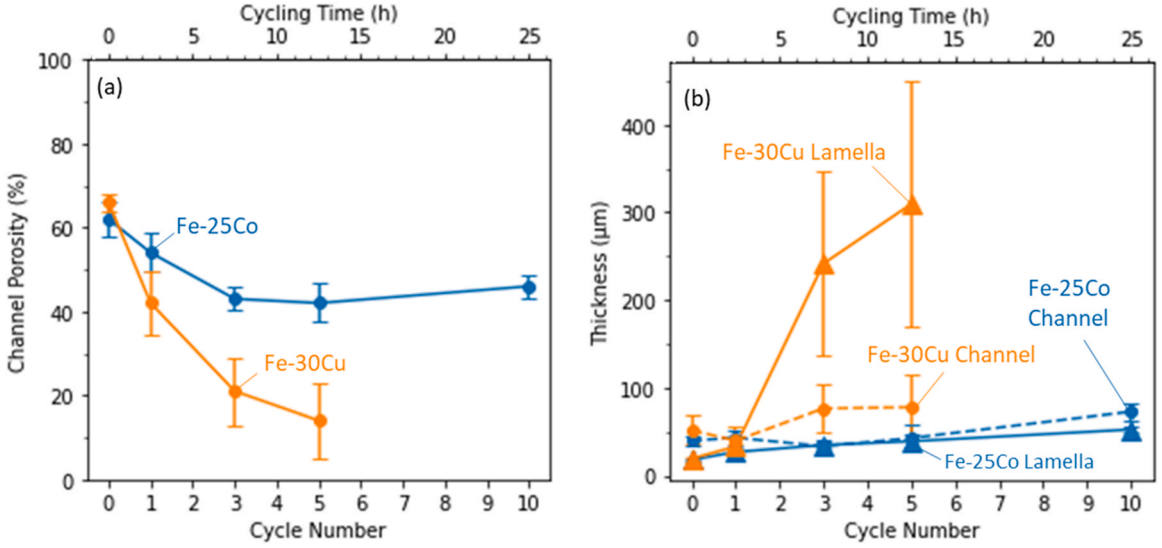

Fig. 12. Evolution with redox cycle number of (a) channel (interlamellar) porosity and (b) lamellar and channel thickness for Fe-25Co (blue) and Fe-30Cu (orange) foam. Fe-30Cu data extends only to 5 cycles, when total densification occurs.

latter value may be an overestimate, as individual channels are not visible after 5 cycles (Fig. 11c), and coarsened micropores within the partially sintered Fe-30Cu matrix may in fact have been misidentified as choked channels. In the Fe-25Co foam, by contrast, the channel porosity decreases slowly from the first to the third cycle, and then remain constant to the fifth and tenth cycle. This reflects inhibition of lamellar sintering as Co-rich core maintains the shape and orientation of the lamellae as they expand and contract during the redox cycles.

The unexpected result of channel thickness increasing for Fe-30Cu foams between 1 and 3 cycles is due to the filtering of micropores during image processing: since most channels have been closed or nearly closed, many channels' thicknesses are below the threshold for micropores (as illustrated in Fig. 11(e–f)). These nearly fully densified channels are then excluded from further channel analysis since they cannot be distinguished from Kirkendall microporosity. The few swollen channels do not collapse with further cycling, as densified regions separate from each other, leaving large voids in the sample center. The Fe-30Cu lamellae simultaneously grow increasingly thick as neighboring lamellae buckle, sinter, and densify. In the Fe-25Co foam, on the other hand, the number of channels and lamellae does not change significantly, and their thickness are mostly stable over the first ten cycles. This reflects both the buckling inhibition and fracture prevention provided by the Co-rich core during oxidation, preserving the original lamellar morphology and microstructure.

4. Conclusions

The effects of alloying additions to Fe, upon the degradation mechanisms of Fe-rich lamellar foams during redox cycling, has been explored for (i) Co, an element highly soluble in Fe (like previously-studied Ni) and (ii) Cu, an element insoluble in Fe. Neither Co nor Cu form oxides during steam oxidation used here, unlike Fe which forms Fe_3O_4. The microstructural and morphological evolution, as well as the reaction kinetics, of Fe-25Co and Fe-30Cu (at%) foams are studied, with the following main conclusions.

4.1. Fe-25Co foams

(1) During oxidation, Co is rejected into lamellar interiors by the growing Fe_3O_4 scale on the lamellae surfaces, to form a fcc-Co (Fe) core. Fracture within the lamellae is inhibited, possibly because of better oxide/metal adhesion. Furthermore, the core formation eliminates most Kirkendall pores forming during the oxidation of Fe lamellae in pure Fe foams, consistent with fast diffusion of Co in Fe. Microporosity is however still induced by the oxidation of microchannels present within lamellae from the sintering step during foam fabrication.
(2) Upon reduction, the fcc-Co(Fe) core catalyzes and accelerates the oxide reduction reaction. The high solubility and fast diffusion of Co in Fe allow the newly reduced metallic Fe to homogenize with the fcc-Co(Fe) core, while enhancing sintering of small pores after each cycle.
(3) The microstructural changes of Fe-25Co lamellae during a redox cycle are reversible, so that the channel and lamellar dimensions are stable over ten redox cycles.

4.2. Fe-30Cu foams

(4) Upon oxidation, pure Cu forms a core within the lamellae due to its rejection by the expanding Fe_3O_4 scale. However, since Cu is insoluble in Fe, this core does not re-homogenize with newly formed Fe during reduction (as Co does), nor does it provide any mitigation of Kirkendall porosity growth. Lamellae often split and buckle, leading to rapid densification of the foam structure.
(5) The time necessary for complete oxidation is half that for pure Fe foam, indicating a kinetic benefit from the Cu on Fe oxidation.
(6) The time for reduction is also decreased as compared to pure Fe foams: Cu, like Co, catalyzes the reduction of Fe_3O_4 and FeO to Fe.

Overall, Ni, Co and Cu additions to Fe highlight the importance of the following factors to decrease damage accumulation during redox cycling:

(i) Alloying with an element which is soluble in Fe and which does not oxidize under steam (such as Ni or Co) enables chemical re-homogenization during reduction, after the alloying element is segregated at the lamellar core during Fe oxidation.

(ii) Maintaining a tough and ductile metallic core within each lamella during oxidation prevents lamellar fracture, as achieved with Co and Ni, which do not oxidize under steam and adhere to the Fe_3O_4 layer;.

(iii) Accelerating Fe redox kinetics is achieved both during oxidation (with Cu) and reduction (with Ni, Co and Cu).

CRediT authorship contribution statement

Samuel Pennell: Investigation, Writing – original draft, Writing – review & editing, Visualization, Validation. **Jacob Mack:** Investigation, Writing – review & editing, Software, Validation, Visualization. **David Dunand:** Conceptualization, Supervision, Funding acquisition, Writing – review & editing.

Declaration of Competing Interest

The authors declare the following financial interests/personal relationships which may be considered as potential competing interests: David Dunand reports financial support was provided by National Science Foundation. David Dunand reports a relationship with Cell Mobility Inc that includes: consulting or advisory and equity or stocks.

Acknowledgements

The research was funded by U.S. National Science Foundation under grant 2015641. The authors acknowledge Dr. Christos Malliakas (NU) for assistance with XRD experiments, Dr. Christoph Kenel (NU) for help with XRD analysis, and Dr. Stephen Wilke (Materials Development, Inc.) for insightful discussions. This work made use of (i) NU's IMSERC X-ray facility which has received support from the Soft and Hybrid Nanotechnology Experimental (SHyNE) Resource (NSF ECCS-2025633), and Northwestern University and (ii) the MatCI Facility supported by the MRSEC program of the National Science Foundation (DMR-1720139) at NU's Materials Research Center.

Appendix A. Supporting information

Supplementary data associated with this article can be found in the online version at doi:10.1016/j.jallcom.2022.165606.

References

[1] C. Wang, et al., Recent progress of metal–air batteries—a mini review, Appl. Sci. 9 (14) (2019) 2787.
[2] D. Ahuja, V. Kalpna, P.K. Varshney, Metal air battery: a sustainable and low cost material for energy storage, J. Phys. Conf. Ser. 1913 (1) (2021) 012065.
[3] X. Zhang, et al., Recent progress in rechargeable alkali metal-air batteries, Green Energy Environ. 1 (1) (2016) 4–17.
[4] H.F. Wang, Q. Xu, Materials design for rechargeable metal-air batteries, Matter 1 (3) (2019) 565–595.
[5] R.D. McKerracher, et al., A review of the iron-air secondary battery for energy storage, ChemPlusChem 80 (2) (2015) 323.

[6] A. Dinesh, et al., Iron-based flow batteries to store renewable energies, Environ. Chem. Lett. 16 (3) (2018) 683–694.
[7] C.J. Zhang, K. Huang, A comprehensive review on the development of solid-state metal-air batteries operated on oxide-ion chemistry, Adv. Energy Mater. 11 (2021) 2.
[8] N. Xu, et al., A novel solid oxide redox flow battery for grid energy storage, Energy Environ. Sci. 4 (12) (2011) 4942–4946.
[9] X. Zhao, et al., Cyclic durability of a solid oxide Fe-air redox battery operated at 650C, J. Electrochem. Soc. 160 (10) (2013) A1716.
[10] X. Zhao, et al., Performance of solid oxide iron-air battery operated at 550C, J. Electrochem. Soc. 160 (8) (2013) A1241.
[11] X. Zhao, et al., Enhanced reversibility and durability of a solid oxide Fe–air redox battery by carbothermic reaction derived energy storage materials, Chem. Commun. 50 (5) (2014) 623–625.
[12] H. Ohmori, H. Iwai, Simulation of solid oxide iron-air battery: effects of heat and mass transfer on charge/discharge characteristics, J. Power Sources 286 (2015) 264–275.
[13] X. Jin, et al., Energy efficiency of an intermediate-temperature solid oxide iron–air redox battery, J. Energy Storage 3 (2015) 1–9.
[14] S. Trocino, et al., High performance solid-state iron-air rechargeable ceramic battery operating at intermediate temperatures (500-650 degrees C), Appl. Energy 233 (2019) 386–394.
[15] W.W. Drenckhahn, et al., A novel high temperature metal - air battery, ECS Trans. 50 (45) (2013) 125–135.
[16] P.J. Lloreda-Jurado, et al., Pore morphology evolution and atom distribution of doped Fe2O3 foams developed by freeze-casting after redox cycling, J. Mater. Res. Technol. (13) (2021) 1887–1898.
[17] C. Dueso, C. Thompson, I. Metcalfe, High-stability, high-capacity oxygen carriers: iron oxide-perovskite composite materials for hydrogen production by chemical looping, Appl. Energy 157 (2015) 382–390.
[18] C.M. Berger, et al., Development of storage materials for high-temperature rechargeable oxide batteries, J. Energy Storage 1 (2015) 54–64.
[19] A. Leonide, et al., Long term operation of rechargeable high temperature solid oxide batteries, J. Electrochem. Soc. 161 (9) (2014) A1297–A1301.
[20] K. Otsuka, et al., Chemical storage of hydrogen by modified iron oxides, J. Power Sources 122 (2) (2003) 111–121.
[21] A.A. Plunk, D.C. Dunand, Iron foams created by directional freeze casting of iron oxide, reduction and sintering, Mater. Lett. 191 (2017) 112–115.
[22] S.K. Wilke, D.C. Dunand, In operando tomography reveals degradation mechanisms in lamellar iron foams during redox cycling at 800° C, J. Power Sources 448 (2020) 227463.
[23] P.J. Lloreda-Jurado, et al., Structure–processing relationships of freeze-cast iron foams fabricated with various solidification rates and post-casting heat treatment, J. Mater. Res. 35 (19) (2020) 2587–2596.
[24] K.L. Scotti, D.C. Dunand, Freeze casting – a review of processing, microstructure and properties via the open data repository, FreezeCasting.net, Prog. Mater. Sci. 94 (2018) 243–305.
[25] E. Munch, et al., Architectural control of freeze-cast ceramics through additives and templating, J. Am. Ceram. Soc. 92 (7) (2009) 1534–1539.
[26] S.K. Wilke, D.C. Dunand, Fe–Ni foams self-heal during redox cycling via reversible formation/homogenization of a ductile Ni scaffold, J. Mater. Chem. A 8 (37) (2020) 19375–19386.
[27] S.K. Wilke, D.C. Dunand, Structural evolution of directionally freeze-cast iron foams during oxidation/reduction cycles, Acta Mater. 162 (2019) 90–102.
[28] C.D. Bohn, et al., Stabilizing iron oxide used in cycles of reduction and oxidation for hydrogen production, Energy Fuels 24 (7) (2010) 4025–4033.
[29] W. Zhang, et al., Thermodyn. Anal. Iron Oxides Redox React., PRICM (2013) 777–789.
[30] C. Stolze, et al., Directional solidification with constant ice front velocity in the ice-templating process, Adv. Eng. Mater. 18 (1) (2016) 111–120.
[31] Zhang, W., et al. Thermodynamic analyses of iron oxides redox reactions, in: Proceedings of the Eighth Pacific Rim International Congress on Advanced Materials and Processing, Springer, 2013.
[32] R. Dougherty, K.-H. Kunzelmann, Computing local thickness of 3D structures with ImageJ, Microsc. Microanal. 13 (S02) (2007) 1678–1679.
[33] S.K. Wilke, et al., Evolution of directionally freeze-cast Fe2O3 and Fe2O3+NiO green bodies during reduction and sintering to create lamellar Fe and Fe-20Ni foams, J. Alloy. Compd. 889 (2022) 161707.
[34] C. Kenel, M.M.F. Al Malki, D.C. Dunand, Microstructure evolution during reduction and sintering of 3D-extrusion-printed Bi2O3+TeO2 inks to form Bi2Te3, Acta Mater. 221 (2021) 117422.
[35] K.M. Thyng, et al., True colors of oceanography: guidelines for effective and accurate colormap selection, Oceanography 29 (3) (2016) 9–13.
[36] S. ROWLAND, J. Rook, Analytical methods, Int. J. Dairy Technol. 14 (3) (1961) 112–114.
[37] Newville, M., et al., LMFIT: non-linear least-square minimization and curve-fitting for Python, Astrophysics Source Code Library, 2016,. ascl: 1606.014.
[38] Hoyt, J.J., Phase transformations, 2011: McMaster University Bookstore.
[39] Mack, J.B., S.M. Pennell, D.C. Dunand, Microstructural Evolution of Fe-25Ni Lamellar Foams during Redox Cycling, 2021.
[40] A.V. Khvan, et al., Thermodynamic assessment of the Cu-Fe-O system, J. Phase Equilib. Diffus. 32 (6) (2011) 498–511.
[41] W. Luc, et al., Role of surface oxophilicity in copper-catalyzed water dissociation, ACS Catal. 8 (10) (2018) 9327–9333.
[42] F.-X. Chiron, G.S. Patience, Kinetics of mixed copper–iron based oxygen carriers for hydrogen production by chemical looping water splitting, Int. J. Hydrog. Energy 37 (14) (2012) 10526–10538.
[43] Q. Lu, et al., Highly porous non-precious bimetallic electrocatalysts for efficient hydrogen evolution, Nat. Commun. 6 (1) (2015) 6567.
[44] H. Bahzad, et al., Iron-based chemical-looping technology for decarbonising iron and steel production, Int. J. Greenh. Gas Control 91 (2019) 102766.
[45] Jones, N., A Study of the Oxidation of FeCo Alloys and their Resulting Magnetic Properties, 2011.
[46] C.H.F. Peden, K.B. Kidd, N.D. Shinn, Metal/metal-oxide interfaces: a surface science approach to the study of adhesion, J. Vac. Sci. Technol. A 9 (3) (1991) 1518–1524.
[47] Brandes, E.A. , G. Brook, Smithells Metals Reference Book, 2013, Elsevier.